ACS APPLIED MATERIALS & INTERFACES

Research Article

www.acsami.org

Shape-Selective Dependence of Room Temperature Ferromagnetism Induced by Hierarchical ZnO Nanostructures

D. E. Motaung,*[,†] G. H. Mhlongo,*[,†] S. S. Nkosi,*[,‡] G. F. Malgas,[§] B. W. Mwakikunga,[†] E. Coetsee,[∥] H. C. Swart,[∥] H. M. I. Abdallah,[⊥] T. Moyo,[⊥] and S. S. Ray[†]

[†]DST/CSIR Nanotechnology Innovation Centre, National Centre for Nano-Structured Materials, Council for Scientific and Industrial Research, P.O. Box 395, Pretoria 0001, South Africa

[‡]CSIR-National Laser Centre, 626 Meiring Naude Rd., Brummeria, Pretoria 0001, South Africa

[§]Department of Physics, University of the Western Cape, Private Bag X17, Bellville 7535, South Africa

[∥]Department of Physics, University of the Free State, P.O. Box 339, Bloemfontein ZA9300, South Africa

[⊥]School of Chemistry and Physics, Westville Campus, University of KwaZulu-Natal, Private Bag X54001, Durban 4000, South Africa

Supporting Information

ABSTRACT: We report on the room temperature ferromagnetism of various highly crystalline zinc oxide (ZnO) nanostructures, such as hexagonally shaped nanorods, nanocups, nanosamoosas, nanoplatelets, and hierarchical nano "flower-like" structures. These materials were synthesized in a shape-selective manner using simple microwave assisted hydrothermal synthesis. Thermogravimetric analyses demonstrated the as-synthesized ZnO nanostructures to be stable and of high purity. Structural analyses showed that the ZnO nanostructures are polycrystalline and wurtzite in structure, without any secondary phases. Combination of electron paramagnetic resonance, photoluminescence, and X-ray photoelectron spectroscopy studies revealed that the zinc vacancies (V_{Zn}) and singly ionized oxygen vacancies (V_O^+) located mainly on the ZnO surface are the primary defects in ZnO structures. A direct link between ferromagnetism and the relative occupancy of the V_{Zn} and V_O^+ was established, suggesting that both V_{Zn} and V_O^+ on the ZnO surface plays a vital role in modulating ferromagnetic behavior. An intense structure- and shape-dependent ferromagnetic signal with an effective *g*-value of >2.0 and a sextet hyperfine structure was shown. Moreover, a novel low field microwave absorption signal was observed and found to increase with an increase in microwave power and temperature.

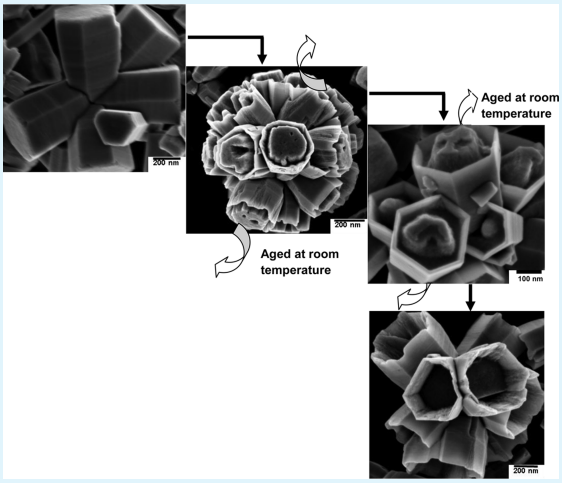

KEYWORDS: *ZnO, hydrothermal synthesis, morphology, magnetic properties*

1. INTRODUCTION

Metal oxide (MOX) semiconductors play important roles in many areas of chemistry, physics and materials science. Among metal oxides, zinc oxide (ZnO) is a semiconductor with a direct band gap energy of 3.37 eV at room temperature and a relatively large binding energy (60 meV).[1] ZnO crystallizes in a wurtzite structure and exhibits *n*-type electrical conductivity. Due to the inexpensive and simple synthesis routes of its various nanostructures, ZnO is widely used as a semiconductor in solar cells, luminescent materials, transparent conductors, and gas sensors.[2,3]

Recently, research has shifted into transition metal−ZnO diluted magnetic oxides (DMOs). The increased interest in these materials is due not only to their promise in spintronic applications but also to their excellent physical and structural properties. Diverse magnetic properties have been observed experimentally in ZnO-based diluted magnetic semiconductors (DMSs).[4−7] Several different theoretical models have been developed to explain the coupling mechanism responsible for the observed room-temperature ferromagnetism (RTFM).[8,9] However, the basis of RTFM in DMS is not fully understood, and the mechanism behind the magnetic ordering is still a topic of discussion. Additionally, despite some initial promising results on DMS, it is not clear if they can exhibit this required high-temperature magnetism, that is, Curie temperatures (T_C) above 300 K, in order to be useful for technological applications.[4−7] Furthermore, above all the outstanding previous work, no evidence for ferromagnetic order in the transition metal atoms in Co- and Mn-doped ZnO systems was demonstrated.[10−12] In addition, several recent reports claimed the observation of FM in semiconductor and insulating oxide nanostructures without any doping despite the diamagnetic

Received: August 16, 2013
Accepted: May 20, 2014
Published: May 20, 2014

character of the material in bulk.[9,14−19] To date, several types of defects, such as oxygen and zinc vacancies, as well as hydrogen, oxygen, and zinc interstitials, have been proposed by different researchers to induce RTFM in ZnO-based nanostructures.[13−19] The desire to clarify the origin of these defects and to provide an explicit coupling mechanism behind RTFM in undoped ZnO has inspired extensive experimental and theoretical research.[19−22] It has, however, proven difficult to uncover a direct link between magnetization and defects due to the complexity of the defect states in the ZnO structure.

Irrespective of the great body of research achieved to date in this type of systems (both doped and undoped), there is still a strong controversy regarding its origin and whether the FM is intrinsic or due to extrinsic origins, such as magnetic metal clusters, secondary phases, or contaminants. As a result, advanced characterization tools such as X-ray absorption spectroscopy (XAS) and X-ray magnetic circular dichroism (XMCD) are critical into determining if the RTFM behavior, as determined from macroscopic magnetometry, is intrinsic or extrinsic.[10,22,23]

Recently, Barla et al.[23] revealed that the RTFM found in bulk magnetization measurements of Co:ZnO DMS was not due to Co, whose 3d states showed paramagnetic behavior according to magnetic probes as XMCD. Keavney et al.[24] probed the XMCD at the Cu(3d), O(2p), and Zn(3d) states and found no dichroic signal consistent with FM originating from any of these states. Hence, only a paramagnetic (PM) component was detected at the Cu(3d), and no magnetic signal in the O or Zn was observed, denoting that the 3d electronic shells of the cations in these DMS do not carry any measurable ferromagnetic moment. Therefore, these results rule out the possibility of RTFM being due to extrinsic effects associated with 3d cations. However, regarding whether the FM is really intrinsic, recently, XMCD analyses carried out on ZnO nanoparticles (NPs) capped with organic molecules and without any 3d doping have revealed the existence of an intrinsic ferromagnetic contribution and suggested that it branches from the interface formed between the ZnO core of the NP and the capping region created by bonding to the organic molecules.[25−27]

To the best of our knowledge, there are no reports on low field microwave absorption (LFMA), RTFM, or sextet hyperfine structures in shape-selective ZnO nanostructures with different morphologies, such as nanosamoosas, nanoplatelets, hierarchical nanoflowers, and nanocups. Here, we report novel LFMA and RTFM observed for various ZnO nanostructures synthesized via a hydrothermal microwave route. By employing photoluminescence, electron paramagnetic resonance, vibrating sample magnetometer, and X-ray photoelectron spectroscopy, we conclusively prove that the observed LFMA, RTFM signal, and sextet hyperfine structures are shape dependent. A direct correlation between the ferromagnetism and the relative concentration of the zinc vacancies (V_{Zn}) and singly ionized oxygen vacancies (V_O^+) is established, suggesting that V_{Zn} and V_O^+ on the ZnO surface play a vital role in modulating ferromagnetic and sextet hyperfine structures. Moreover, our results also show that LFMA and FMR signals increase with increasing microwave power and temperature, signifying that these structures are stable even at higher temperatures, as evident by their high Curie temperatures (T_C > 400 K).

2. EXPERIMENTAL DETAILS

2.1. Synthesis of ZnO Nanostructures. All chemicals were purchased from Sigma-Aldrich and used as received without any further purification. ZnO nanocups, nanoplatelets, nanosamoosas, and hierarchical "flower-like" structures were prepared from aqueous solutions of the Zn^{2+} precursor zinc acetate ($Zn(CH_3COO)_2{\cdot}2H_2O$) (99.99%) with ammonium (NH_4OH) (33% NH_3 in water, 99.99%), lithium hydroxide (LiOH), potassium hydroxide (KOH), and sodium hydroxide (NaOH) used as hydroxide anion precursors. These precursor solutions were mixed in 1:4 molar ratios in 100 mL of distilled water under vigorous stirring. In separate experiments, a few drops of the chosen hydroxide precursor were added into zinc acetate solutions until the desired pH of 8 was reached. The pH was controlled using S220 Seven Compact pH/ion meter. The precursor solutions were continuously stirred for 15 min, transferred into Teflon vessels, and subjected to microwave oven irradiation (Perkin-Elmer/Anton Paar Multiwave 3000) for 10 min at a power of 150 W. A white precipitate fell from the solution, which was collected by filtration and washed several times with absolute ethanol and distilled water to remove undesired impurities. The final product was dried in an oven at 60 °C for 24 h to obtain ZnO nanostructures.

2.2. Characterization Methods. The morphology of the synthesized ZnO nanostructures was evaluated using a high-resolution scanning electron microscopy (HR-SEM, Auriga ZEISS) instrument operated at an accelerating voltage of 3 kV. The internal structures of the ZnO materials were studied by HR-transmission electron microscopy (JEOL TEM-2100). The structural properties and grain size of the materials were investigated using a Panalytical X'pert PRO PW 3040/60 X-ray diffractometer with a Cu Kα (λ = 0.154 nm) monochromated radiation source. Raman spectroscopy was conducted using Horiba Jobin-Yvon HR800 Raman microscope at room temperature with a 514 nm excitation laser and a spectral resolution of 0.4 cm^{-1}. The UV−visible absorption (UV−vis) and photoluminescence (PL) spectra were determined using Perkin-Elmer Lambda 750 UV−vis and Jobin-Yvon NanoLog spectrometers, respectively. Emission was detected with a Jobin-Yvon PMT detector.

The microwave absorption measurements of the as-prepared ZnO samples were carried out using a JEOL X-band electron paramagnetic resonance (EPR) spectrometer (JES FA 200) equipped with an Oxford ESR900 gas-flow cryostat and a temperature control (Scientific instruments 9700). The microwave power was varied between 1 and 30 mW, and the frequency was held at approximately 9.4 GHz. The DC field was modulated with a superposed AC field with constant amplitude. The microwave response was measured as a derivative signal. In this experiment, the temperature was varied between 298 and 450 K. Furthermore, the field dependent magnetic characterization was performed using Lakeshore 735 vibrating sample magnetometer (VSM) at room temperature. It is vital to point out that because this type of sample exhibits small magnetization signals, special care was taken during measurements as to avoid any trace magnetic contamination.[13,28] Magnetic measurements performed on different batches of ZnO powders showed consistent and reproducible results demonstrating RTFM behavior. For detailed analysis on the magnetic measurements, see the Supporting Information. X-ray photoelectron spectroscopy analyses were carried using a PHI 5000 Versaprobe-Scanning ESCA Microprobe. The survey scans were recorded with a 100 μm, 25 W, 15 kV beam using monochromatic Al Kα radiation ($h\nu$ = 1486.6 eV) and for the higher resolution spectra the hemispherical analyzer pass energy was maintained at 11.8 eV (C 1s, O 1s, Zn 2p) for 50 cycles. Measurements were performed using either a 1 eV/step and 45 min acquisition time (binding energies ranging from 0 to 1400 eV) for survey scans or a 0.1 eV/step and 20−30 min acquisition times for the high-resolution scans. The pressure during acquisition was typically under 1×10^{-8} Torr. The surfaces were also sputtered clean for 30 s using an Ar ion gun (2 kV energy ions) and measurements were repeated. Thermogravimetric analysis (TGA) was performed on the ZnO materials using a TA Q500 thermogravimetric analyzer. The measurements were carried out in air with a heating rate of 10 °C/min from room temperature to 950 °C. The sample mass was standardized

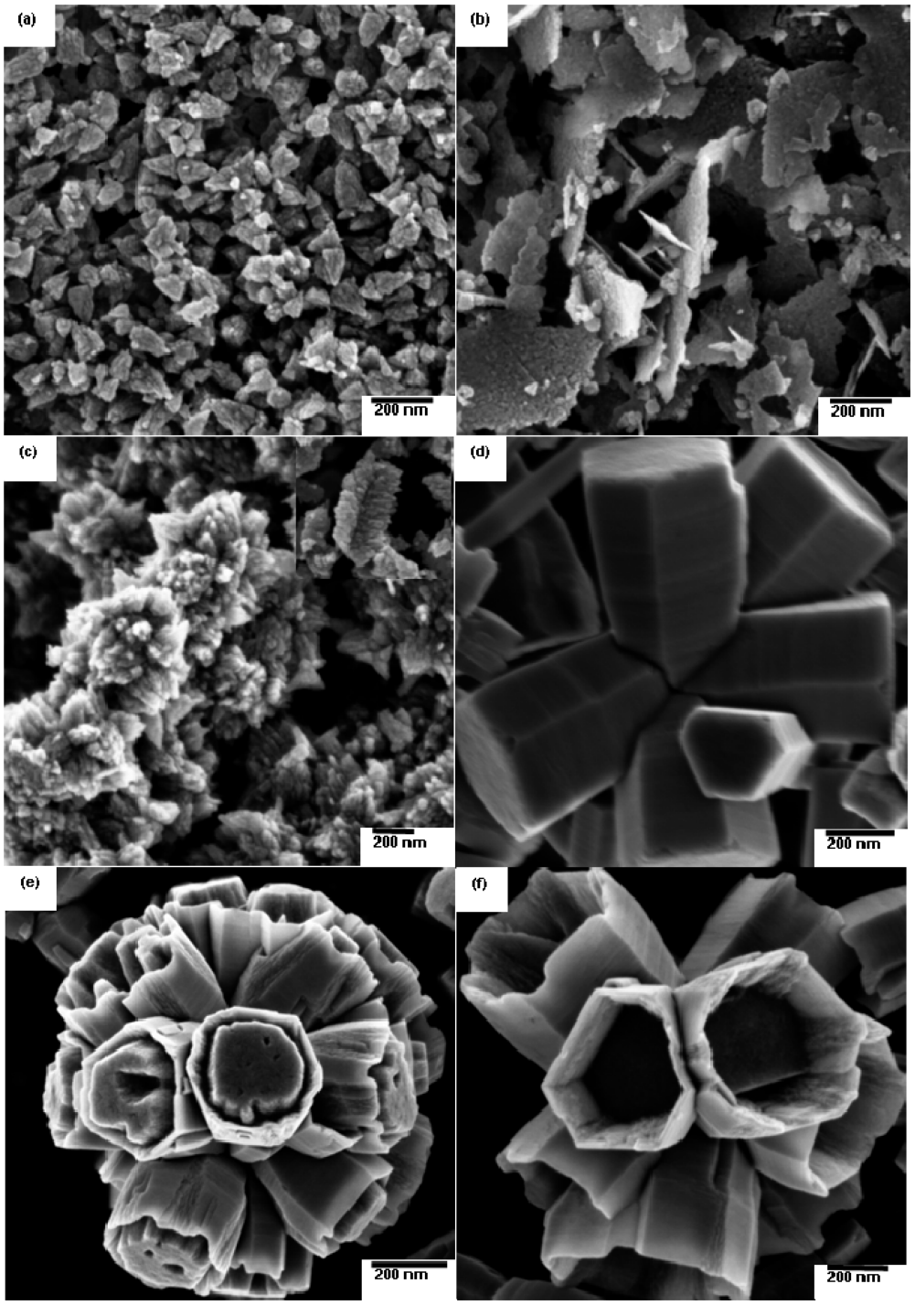

Figure 1. HR-SEM micrographs of the as-synthesized ZnO nanostructures (a) nanosamoosas (b) nanoplatelets (or nanodiscs), (c) hierarchical "flower-like" structure, (d) hexagonal-shaped "flower-like", and (e,f) open and closed nanocups with "flower-like" structure.

at ≈2 mg for all of the measurements to reduce any effect deriving from variation in sample size.

3. RESULTS AND DISCUSSION

The driving force behind the study of shape-selective formation of ZnO nanostructures through hydrothermal assisted synthesis with various bases is the ultimate control of the crystal growth, structure, and morphology. Figure 1 shows high-resolution scanning electron microscopy (HR-SEM) images of the ZnO nanostructures synthesized with different base solutions. Figure 1a shows that the use of KOH yields ZnO with "samoosa-like" structures with diameters and lengths of approximately 50−100 nm and 100−130 nm, respectively. Figure 1b depicts a "platelet-like" or "disc-like" structure synthesized using LiOH as base. These structures have diameters in the range of 150−200 nm and lengths of up to ≈400 nm. These nanoplatelets were generally found intertwined with each other, with a thickness of more than 100 nm. Moreover, the polar surfaces of these nanoplatelets are not clean and are covered with small particles; they also exhibit a granulated, porous structure.

When NaOH solution was used, hierarchical structures with "flower-like" appearances were formed (Figure 1c). These

nanostructures grow outward from the base of the material, forming a "flower-like" array. Figure 1d shows hexagonally shaped ZnO nanorods with a "flower-like" structure synthesized using NH_4OH. These "flower-like" ZnO structures are constructed of dozens of ZnO nanorods radiating out from a common center. These radially oriented ZnO rods have diameters and lengths ranging from 200 to 350 nm and 400 to 600 nm, respectively. Figure 1e,f shows hexagonally shaped ZnO nanorods with both closed and open cavities at their ends. The closed cavity is composed of hexagonal rods, which energy-dispersive X-ray spectroscopy (EDS) analysis revealed to be pure ZnO (see the Supporting Information). The average outer-diameter and length of ZnO nanocups are approximately 350 and 400 nm, respectively.

ZnO flower-like structures are generally synthesized through simple hydrothermal methods. The flowers, which are composed of hexagonal ZnO nanorods, were previously synthesized by Rai et al.[29] using aqueous solutions of zinc nitrate and sodium hydroxide. In the present study, the mechanism for the formation of ZnO nanoflowers with ammonia can be summarized in the following reactions:

$$NH_3 + H_2O \leftrightarrow NH_3{\cdot}H_2O \leftrightarrow NH_4^+ + HO^- \quad (1)$$

$$Zn^{2+} + 4OH^- \rightarrow Zn(OH)_4^{2-} \quad (2)$$

$$Zn^{2+} + 4NH_3 \rightarrow Zn(NH_3)_4^{2+} \quad (3)$$

$$Zn(OH)_4^{2-} \rightarrow ZnO + H_2O + 2OH^- \quad (4)$$

$$Zn(NH_3)_4^{2+} + 2OH^- \rightarrow ZnO + 4NH_3 + H_2O \quad (5)$$

When ammonia–water is used as the hydroxide source, zinc cations readily react to form stable tetrahedral $Zn(OH)_4^{2-}$ and $Zn(NH_3)_4^{2+}$ complexes, which act as the growth units of ZnO structures.[30] The high pH growth of ZnO has been previously shown to be possible with $Zn(OH)_4^{2-}$ and $Zn(NH_3)_4^{2+}$ complexes acting as growth units.[30] A proposed mechanism for the formation of nanocups is shown in Figure 2. During microwave irradiation, temperatures are elevated and ZnO nuclei are formed in the rapid decomposition of $Zn(OH)_4^{2-}$ and $Zn(NH_3)_4^{2+}$. The speed of the precipitation results in the formation of very small ZnO crystals or nuclei. First, ZnO nuclei evolve into hexagonal nanorods by preferential *c*-axis ([0001] direction) oriented growth. Then, multiple hexagonal nanorods growing from the center nuclei result in hexagonally shaped nanoflowers, which are converted into nanocups by a decrease in the crystal growth rate along the [0001] direction and simultaneous local dissolution of the polar (0001) surfaces. While cooling to room temperature over a period of hours, they age, resulting in the formation of complete cups before filtration.

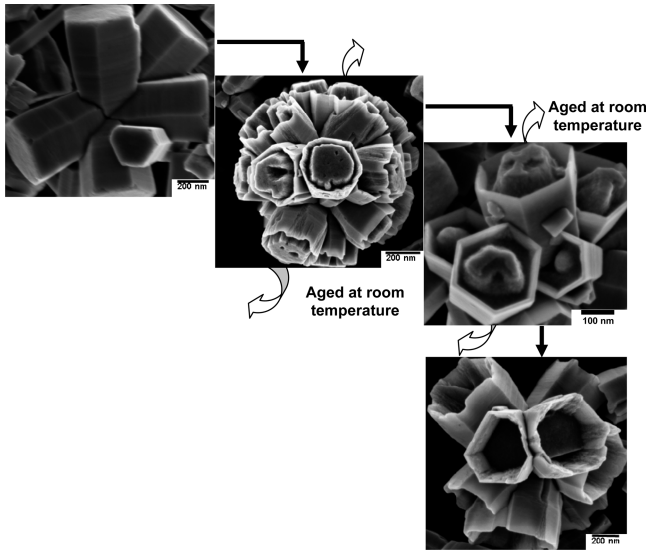

Figure 2. Possible growth mechanism of ZnO structure from hexagonally shaped nanorods to form "cup-like" structure.

To study the structural properties of the samples, X-ray diffraction analyses were carried out. Figure 3 shows the XRD patterns of the as-synthesized ZnO nanostructures with different shapes. All of the peaks correspond to the wurtzite structure of ZnO.[29] No other peaks from impurities or residues are detected, indicating the formation of pure ZnO. As shown in Figure 3, the ZnO nanostructures have similar XRD patterns, with differences in their relative peak intensities due to their random orientation. The strong (002) and (101) diffraction peaks suggest that ⟨002⟩ and ⟨101⟩ are the preferred growth orientations of the ZnO films. The average crystallite sizes, estimated from the XRD patterns of the (002) and (101) peaks, are listed in Table 1.

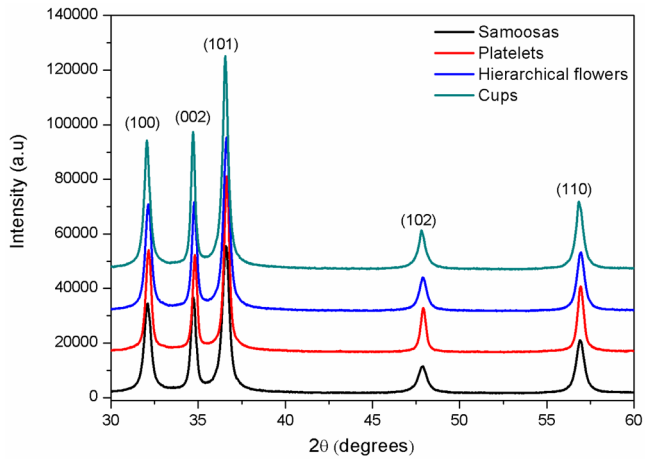

Figure 3. XRD diffraction patterns of the various ZnO nanostructures.

The internal structure of the ZnO products was examined using transmission electron microscopy (TEM) and high-resolution (HR)-TEM (Figure 4). The TEM micrograph in Figure 4a confirms the formation of the "samoosa-like" structure observed by SEM analysis. Their corresponding selected area electron diffraction (SAED) pattern, shown in the inset of Figure 4b, indicates that the "samoosa-like" structures are polycrystalline in nature and are indexed as the hexagonal ZnO phase in accordance with the XRD data.[29] The ZnO sample in Figure 4c consists primarily of "flower-like" nanorods with diameters of 200–350 nm and lengths of 400–500 nm. The HR-TEM image and SAED pattern in Figure 4d indicate a ZnO nanorod in the "flower-like" structure, with clear lattice fringes at a *d*-spacing of 0.26 nm, corresponding to the (002) lattice plane of hexagonal ZnO. These measurements confirmed that the ZnO nanorods of the "flower-like" structures are single crystalline and grow along the direction of the (002) plane. Figure 4e shows TEM image of hexagonally shaped ZnO with a "cup-like" structure, while the lattice fringes

Table 1. Variations of Crystallite Size and Energy Band Gap of the As-Synthesized ZnO Nanostructures

	crystallites size (nm)			
materials	(002)	(101)	optical band gap (eV)	fwhm of E_{2H} mode (cm^{-1})
samoosas	24.82 ± 0.27	17.76 ± 0.13	3.04 ± 0.01	12.29 ± 0.68
platelets	29.55 ± 0.37	23.84 ± 0.98	2.94 ± 0.07	10.43 ± 0.53
hierarchical flower	26.28 ± 0.32	19.77 ± 0.12	2.99 ± 0.06	11.16 ± 0.55
cups	30.38 ± 0.12	22.26 ± 0.53		11.09 ± 0.43

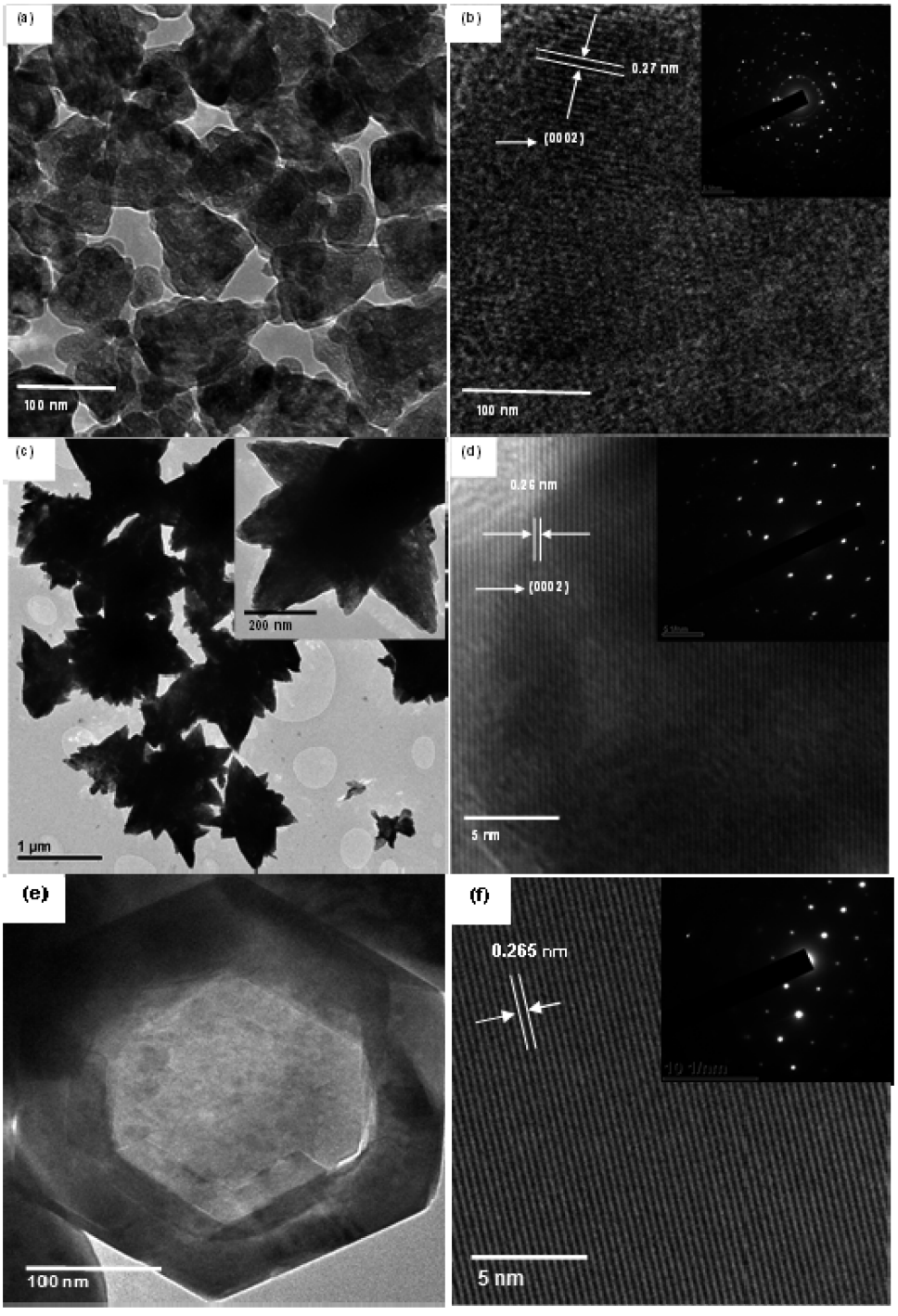

Figure 4. TEM/HR-TEM images of the typical ZnO morphologies: (a,b) samoosa-like structures and their corresponding SAED pattern (inset), (c,d) nanorods composing the ZnO "flower-like" structure and corresponding SAED pattern (inset), (e,f) ZnO "cup-like" structure and corresponding SAED pattern (inset).

at a *d*-spacing of 0.265 nm, corresponding to the (002) lattice plane, are depicted in Figure 4f. The inset in Figure 4f confirms that the hexagonally shaped "cup-like" structures are single crystals and are grown along the *c*-axis direction.

Another effective approach to investigate the phase and purity of the nanostructures is Raman scattering. ZnO has a wurtzite structure displaying 6 mm symmetry and belonging to the C_{6v}^4 space group.[31] The symmetry of the structure governs whether vibrations are Raman active and appear in the spectra, whereas factors such as lattice spacing and chemical environment determine the placement of vibrational frequencies. As shown in Figure 5, the presence of a sharp, strong, nonpolar

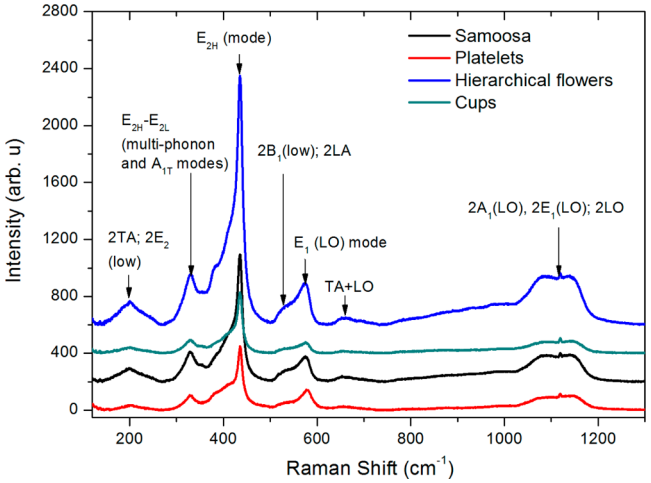

Figure 5. Raman spectra of the as-synthesized ZnO nanostructures.

optical phonon E_{2H} mode at 438 cm^{-1} confirms that the products are wurtzite hexagonal ZnO structure, with full width at half maximum (fwhm) values in the range of 10−13 cm^{-1} (Table 1). Due to size effect, the Raman bands become much smaller. The presence of a high intensity E_2 mode and weak E_1 (LO) mode in the spectrum of ZnO structures indicated increased Raman scattering due to good crystal quality, a result that was consistent with XRD results. Two very small peaks observed at 332 and 376 cm^{-1} are assigned as the E_{2H}−E_{2L} (multiphonon) and A_{1T} modes; respectively.[32] The small shoulder observed at approximately 537 cm^{-1} corresponds to the $2B_1$ (low) and 2LA phonon modes. The E_1 (LO) mode of crystalline ZnO at 583 cm^{-1} is derived from the formation of defects of oxygen vacancies.[33] It can be seen that the intensity of the peak at 583 cm^{-1} is improved for the ZnO with "samoosa-like" and "hierarchical flower-like" structures, indicating high oxygen defects within the ZnO surface. In addition to the typical vibration modes of ZnO, there are two weak-intensity modes at 533 and 660 cm^{-1}, which can be designated as the F_{2g} (2) and A_{1g} modes of Zn_2, respectively. The low intensity Raman bands in the region of 1030−1200 cm^{-1} are attributed to optical overtones and are associated with second-order Raman active modes.[33]

To study the defect structure of the various ZnO nanomaterials, photoluminescence (PL) was employed (Figure 6). The PL of the ZnO materials originates from either the exciton recombination or intrinsic defects.[34] It is evident from Figure 6 that all the ZnO nanomaterials display an ultraviolet (UV) near-band-edge (NBE) emission at 3.3−3.4 eV (≈385 nm) and a blue emission band around 2.9 eV (418 nm). The blue luminescence is assigned to electronic transitions from the Zn interstitial levels (Zn_i) to the valence band,[35] as its peak energy (2.9 eV) is in good agreement with the calculated energy difference between the Zn_i levels and the top of the valence band (2.9 eV).[36] It is worthy to point out that the strong violet-blue emission centered at 445 nm is observed for the ZnO nanoplatelets. Studies revealed that the violet-blue emission is strongly related to the interstitial zinc in the ZnO.[34,37] It is observed in Figure 6 that all the ZnO structures reveal a defect related green-orange band (480−695 nm). It can be seen that this emission shifts as the particle size as well as the shape changes. The origin of broad-band emission is, however, controversial and several kinds of defects and vacancies are found to be responsible for this emission.[34,38] Typically, the reported defects present in ZnO-based nanostructures are oxygen vacancies with different charged states, zinc vacancies, zinc interstitial, and adsorbed molecules.[18,39,40] Djurisic et al.[40] indicated that the resulting defect-related emissions for these mentioned defects normally occur near the blue-green (∼480−550 nm), yellow (∼550−610 nm), and orange-red (∼610−750 nm) regions. To understand the role of individual defects on the magnetic properties of the ZnO nanostructures, a three-peak (Gaussian) fitting method on the broad visible emission was adopted. Thus, deconvoluted spectra in Figure 6b,c show three peaks around 529, 580, and 650 nm for the hierarchical structures, whereas the "samoosa-like" structures only show emissions at higher wavelengths, 544, 613, and 690 nm. The green emission around 529 nm is generally attributed to the recombination of electrons trapped in singly ionized oxygen vacancies (F^+ center or V_O^+) with photogenerated holes[18,41] or the zinc vacancies (V_{Zn}).[42] Studies indicated that the V_{Zn} can also give rise to the green luminescence, which is centered between ∼518 nm (2.4 eV) and ∼495 nm (2.5 eV).[43,44] The PL emissions around 560 and 612 nm are related to the doubly ionized oxygen vacancy (F^{+2} center or V_O^{+2})[18,45] and oxygen interstitials (O_i),[46] respectively. Furthermore, from Figure 6d,e, "cup-like" structures show a PL around 525 and 600 nm, whereas the "platelet-like" structures reveal an emission around 575 and 650 nm. On the basis of the PL intensity, we can conclude that "samoosa" and "hierarchical flower" contain more of the V_{Zn} and V_O^+ than their counterparts, "platelet" and "cup-like" structures.

Figure 7 shows the UV−vis absorption spectra of different ZnO nanostructures. The absorption spectra of the nano-samoosas, platelets, and hierarchical "flower-like" structures show a well-defined exciton band in the region between 335 and 352 nm, which blue-shifted relative to the bulk exciton absorption (373 nm). This blue shift cannot be due to the quantum confinement effect and its effect is not well-known. However, Chen et al.[47] suggested that the blue shift may be attributed to a surface resonance effect caused by an enhanced surface to volume ratio. A less pronounced absorption peak at approximately 385 nm is observed for the nanocups (see inset, Figure 7a), indicating a red shift relative to bulk ZnO (373 nm). This red shift can be explained by the formation of shallow electronic states inside the band gap as a result of impurities in the lattice. The optical energy gap (E_{gap}) in Figure 7b was derived by assuming a direct electronic transition between the edges of the valence and conduction bands, for which the variation in the absorption coefficient with the photon energy $h\nu$ is given by[48]

$$\alpha(h\nu) = A(h\nu - E_{gap})^{1/2} \quad (6)$$

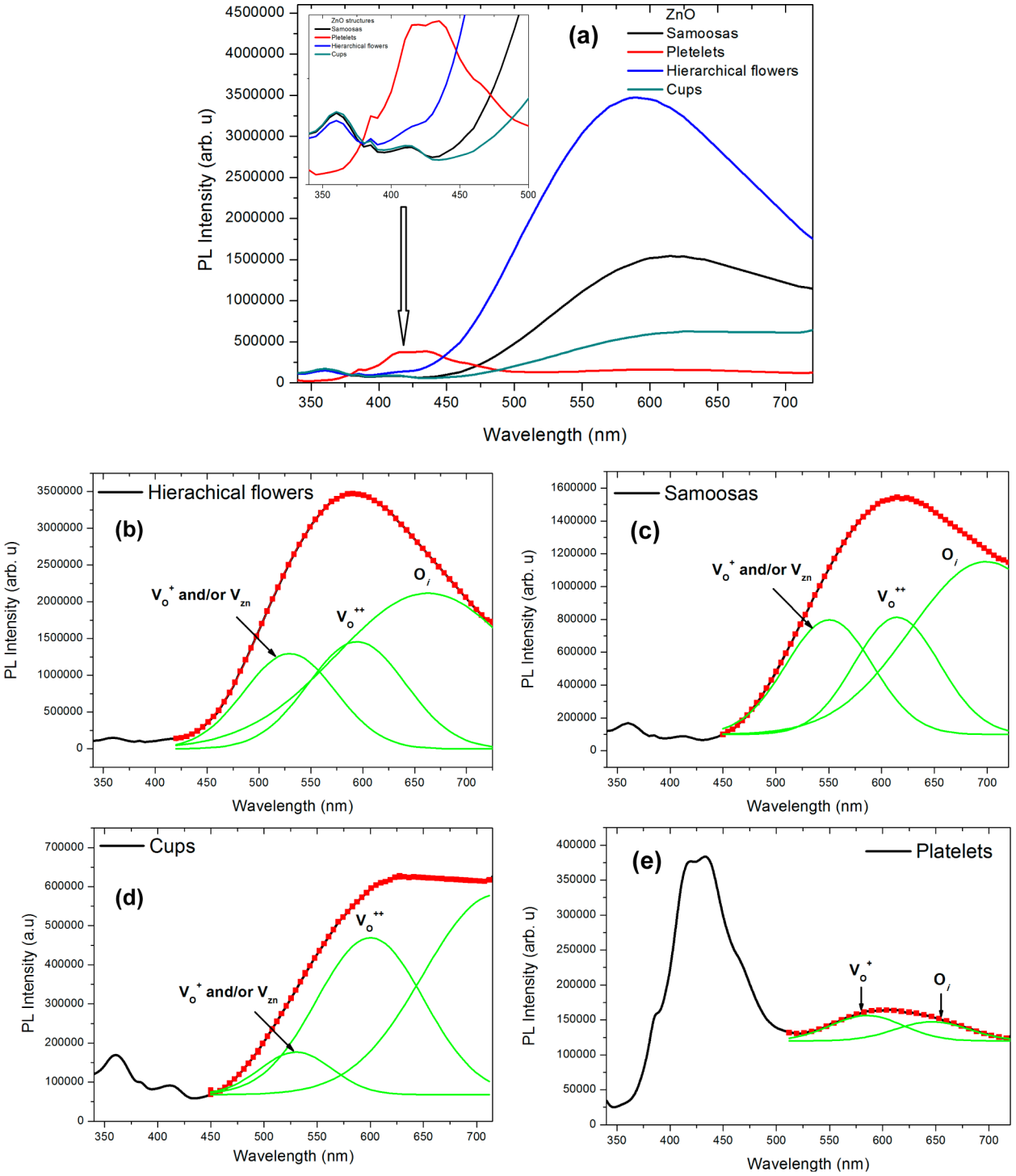

Figure 6. (a) Room-temperature PL spectrum of as-grown ZnO nanostructures, (b–e) Gaussian fits of each PL spectrum (the black lines are the experimental results and the red circles are Gaussian fits).

E_{gap} denotes the optical energy gap between the valence and the conduction band. "Tauc" plots of α^2 versus $h\nu$, given by extrapolation of the linear region of the resulting curve, give a value for E_{gap}. The calculated values of the direct optical energy gap are shown in Table 1.

Electron paramagnetic resonance (EPR) provides a sensitive and direct method to monitor behavior caused by the presence of native defects, such as oxygen and zinc vacancies. To date, most of the experimental investigations of oxygen vacancies in ZnO have relied on EPR measurements. Figure 8 shows the derivative of microwave absorption (dP/dH) as a function of magnetic flux density (DC field) in ZnO nanocrystalline powders recorded at room temperature (T = 293 K) and microwave power of P = 1 mW. Figure 8 exhibits three absorption peaks ($H_{DC} \approx 3$, 300, and 790 mT) associated with three distinct processes. The absorption observed approximately 3 mT is related to low field microwave absorption (LFMA), whereas the broad signal at 300 mT is related to ferromagnetic resonance (FMR) and the feature at 790 mT is due to bulk magnetic defects clusters. LFMA generally

dx.doi.org/10.1021/am501911y | ACS Appl. Mater. Interfaces 2014, 6, 8981–8995

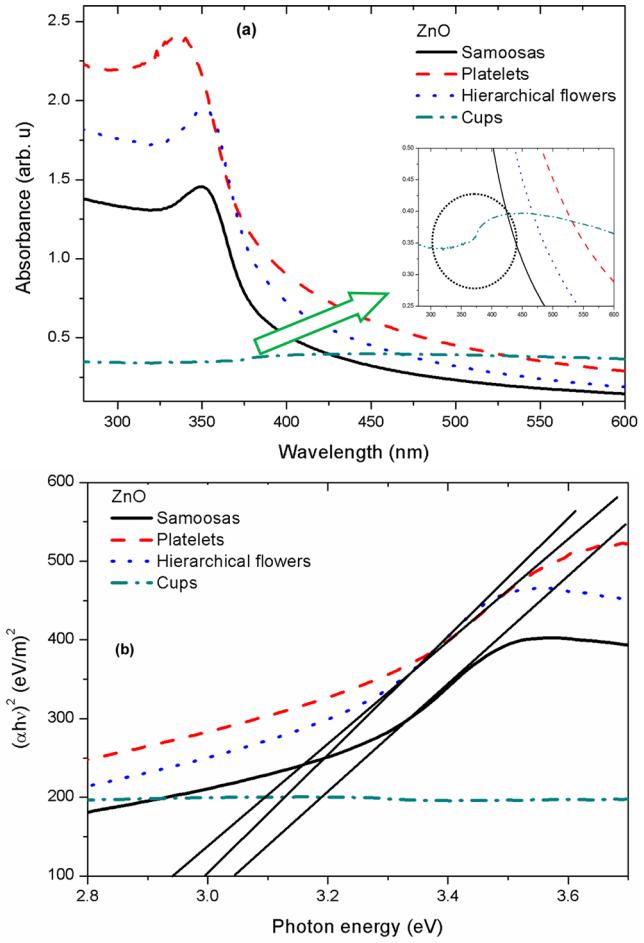

Figure 7. (a) UV/vis absorption spectra and (b) $(\alpha hv)^2$ vs photon energy (hv) plot for the various ZnO nanostructures.

originates from magnetization processes far below saturation. The low field behavior indicates minimum absorption at approximately zero magnetic field, in contrast to the broad absorption for the FMR line. This former signal is understood to be connected to magnetization processes occurring at low field densities. We therefore assume that magnetization is present at relatively low magnetic field as also observed in our case. Such magnetization is attributed to the interaction of the magnetic moments of ZnO with the magnetic field component of electromagnetic radiation at relatively lower field.

The FM observed at 300 mT is due to absorption at full saturation. It is worth noting that the FM spectra of all the as-grown ZnO samples show a unique feature with effective g-factor values at $g \geq 2.0$. A peak with the sextet hyperfine structure is seen approximately 315 mT center field (Figure 8b). This hyperfine structure coupling is attributed to interactions between electronic state and nuclear spin angular momenta in Zn^{2+}. These features could not arise from the manganese (Mn) marker used as a calibration standard in the instrument, as the observed behavior is structure dependent (Figure 8b). Additionally, EDX (see the Supporting Information and XPS, Figure 11) analyses showed no traces of Mn impurities. In addition, Reddy et al.[49] showed that a Mn^{2+} resonance signal with sextet hyperfine structure is observed at $g \approx 2.0$. It is clear from a wide variety of experimental results that magnetism in undoped semiconductor oxide samples should be related to some kind of defects present in the material. So, we assume that both oxygen vacancies such as singly ionized oxygen vacancies (V_O^+) and Zn vacancies (V_{Zn}) are responsible for the room temperature ferromagnetism (RTFM) in ZnO, which also coincides with some previously reported results.[7,15,50] This is due to the fact that as the concentration of V_O^+ or V_{Zn} increases, the ferromagnetic feature also increases. Gosh et al.[17] and Xu et al.[51] also suggested that as the relative concentration of V_O^+ increases, the FM signal also increases. It is worthy to point out that the possibility of a contribution coming from doubly ionized oxygen vacancies (V_O^{+2}) to the magnetization can be ruled out due to the cancellation of two opposite spins (paired electron spins).[18,20] Furthermore, it is interesting to note that the number of spins is higher for the hierarchical "flower-like" and "samoosa-like" structures (Table 2) given that the PL results indicated that they contain more V_O^+ or V_{Zn} content on the ZnO surface (Figure 6) as compared to "platelet and cup-like" structures. It should be noted that the number of spins (N_s) participating in

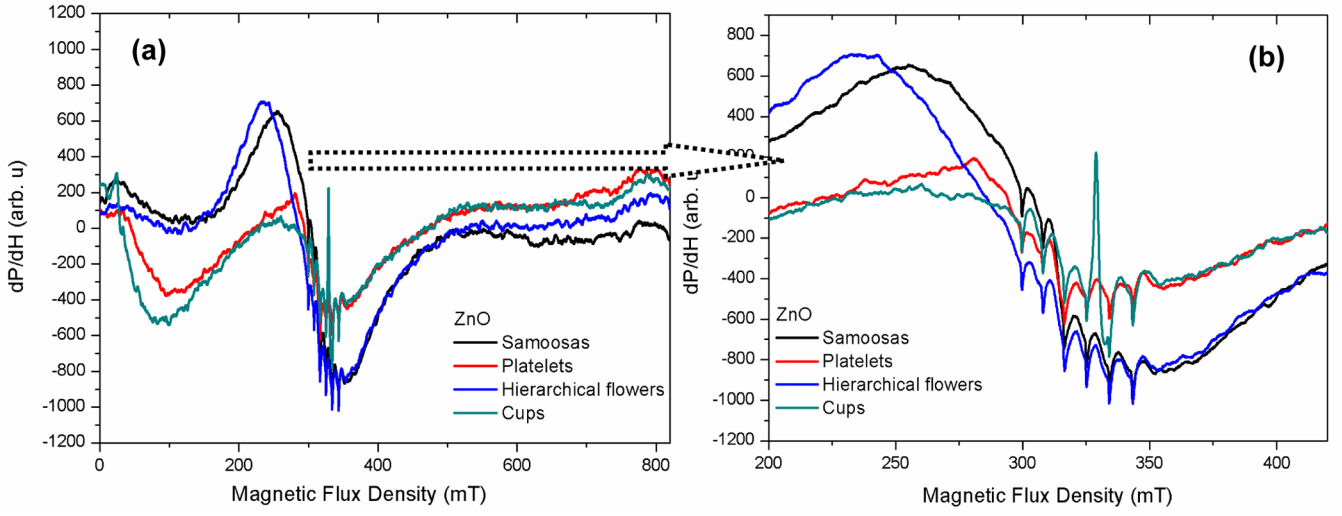

Figure 8. (a) Microwave absorption measurements of various ZnO nanostructures taken at room temperature with a microwave power of 1 mW. Note: (b) corresponds to the inset of Figure 8a.

Table 2. Summary of the FMR, *g*-Factor, ΔH_{EPR} and N_{spins} Extracted from EPR

ZnO structures	FMR field (mT)	*g*-factor	ΔH_{EPR} (mT)	N_{spins} ($\times 10^6$)
samoosas	301.10 ± 1.90	2.1272 ± 0.0035	83.95 ± 4.19	3.09 ± 2.19
platelets	293.95 ± 2.12	2.1788 ± 0.0023	57.99 ± 2.89	0.74 ± 0.51
hierarchical flowers	286.80 ± 3.86	2.2333 ± 0.0570	97.67 ± 4.88	4.66 ± 2.68
cups	281.21 ± 3.94	2.2696 ± 0.0917	60.27 ± 3.01	0.81 ± 0.75

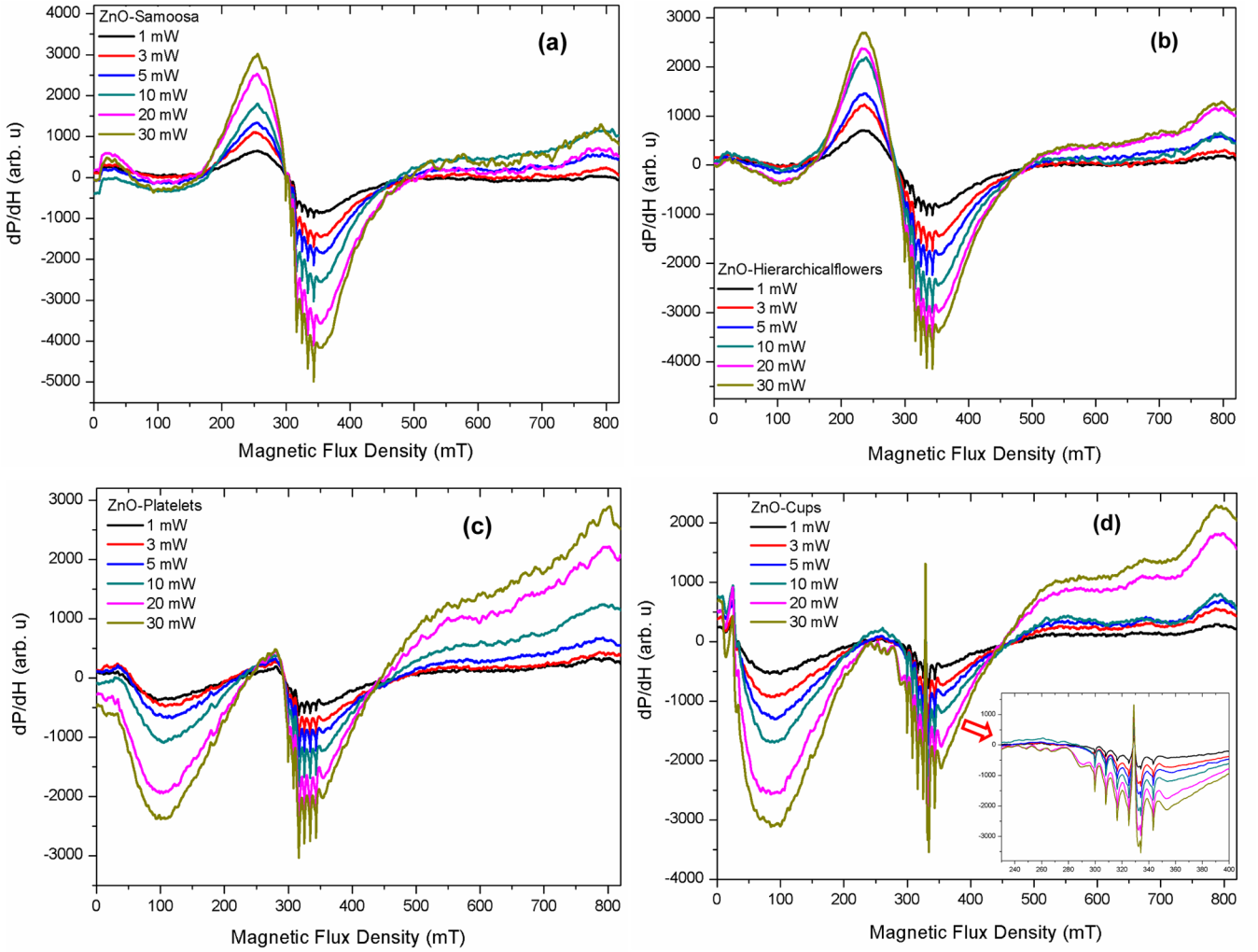

Figure 9. EPR spectra of (a) ZnO−nanosamoosa, (b) hierarchical flowers (c) platelets and (d) "cup-like" structures extracted at different microwave powers. Inset in 9d shows hyperfine structures.

the ferromagnetic ordering resonance can be calculated using the following formula:[52]

$$N_s = 0.285I(\Delta H)^2 \quad (7)$$

here, "*I*" is the peak-to-peak height and ΔH is the line width. Djurišić, et al.[53] showed that broad resonance signals at $g \approx 1.960$ and $g \approx 1.990$ are associated with shallow donors and oxygen vacancies, respectively. Morazzoni et al.[54] attributed two close EPR signals at $g \approx 1.955$ and 1.958 to Zn^+ and V_O^+, respectively. In addition, other studies pointed out that V_O^+ produces the EPR signal $g_\perp = 1.9945$ and $g_\parallel = 1.9960$.[55,56] Moreover, Taylor et al.[57] reported EPR signals with *g*-factors in the range of 2.0018−2.056 in irradiated single crystals related to V_{Zn}, while, Galland et al.[58] observed lines with *g*-factors between 2.0024 and 2.0165 in irradiated single crystals, also attributing them to V_{Zn}. Hence, the assignment of the ESR signals to V_O^+ and V_{Zn} is a rather controversial issue. We therefore speculate that an ESR signal at $g > 2.0$ is related to combination of V_O^+ and V_{Zn} on the ZnO surface. In addition, there is a unique, morphologically independent, intrinsic microwave absorption signal at 790 mT observed in all the nanostructures that can only be excited by high field current. This signal, apparently related to crystal defects inside the bulk, vanishes upon annealing (see the Supporting Information).

Figure 9 shows the variation of the derivative of the microwave absorption with microwave power for various ZnO nanostructures. It can clearly be seen from Figure 9 that ZnO materials with "samoosa-like" and "cup-like" structures show improved LFMA signals with an increase in microwave power. However, a decrease in LFMA signal with microwave power is observed for the "platelet-like" structure, most likely due to its structure or orientation. The observed increase in LFMA with microwave power indicates that variations of microwave

intensity may significantly alter the intensity of the absorption spectra. Experimentally, as microwave power increases, the microwave magnetic field intensity (H_{MW}) in the sample cavity also increases. Gavi et al.[59] showed that the LFMA signal of FeSi increases with increasing microwave power. Interestingly, there is a peculiar signal at approximately 100 mT observed only in ZnO with "platelet-like" and "cup-like" structures. This signal increases as microwave power is increased at the expense of the FMR signal. The nature and origin of this peculiar signal, which is structure/morphology-dependent, is unknown. It is also worth noting that similar behavior is observed at higher magnetic field (790 mT), where the "platelet-like" and "cup-like" structures show enhanced peaks, suggesting that they contain more bulk defects than samoosas and hierarchical flowers.

It is observed in Figure 9a,b that the samoosas and hierarchical "flower-like" structures show enhancements in FMR signal with increasing microwave power. These FMR signals increase with an increase in cavity temperature (see the Supporting Information). The Curie temperature (T_c) for RTFM must be higher for the spintronic applications to be realized. Normally, heating room-temperature ferromagnets will result in magnetic disordering and the loss of ferromagnetism.[60] The observed RTFM suggests that these structures are stable even at higher temperatures, where their magnetism is enhanced rather than dissipated (see the Supporting Information).

Figure 10 shows that the peak-to-peak height and number of spins for various ZnO structures increase with microwave power. It is further observed that the samoosas and hierarchical flowers show improved peak-to-peak height (Figure 10a) and higher numbers of spins (Figure 10b) than the platelets and cups. The higher number of spins (N_s) for samoosas and hierarchical flowers is thought to be due to higher V_{Zn} and V_O^+ on the ZnO surface and reduced crystal sizes (see Table 1). It has been shown previously that larger crystals are detrimental to magnetic properties.[51]

To clarify the origin of RTFM existing in ZnO nanostructures, X-ray photoelectron spectroscopy (XPS) measurements were performed to identify the point defects, Zn−O bonding, and the influence of oxygen on the surface of different ZnO nanostructures. Figure 11 shows a representative broad scan survey spectrum of the ZnO nanostructures. Evidently, only the elements Zn, O, and C are observed and this is consistent with the EDS analysis (see the Supporting Information). The detected carbon is related to the carbon tape used during the measurements and the carbon adsorbed on the surface during the exposure of the sample to the ambient atmosphere. It further excludes the presence of any other impurities.

Figure 12a−d shows the normalized high-resolution XPS scan of the O 1s core level fitted by three Gaussian functions. The higher binding energy peak (O_c) located at about 532.3 eV (O_c) (see Tables 3a and 3b) is attributed to the presence of loosely bound oxygen on the surface of ZnO, belonging to chemisorbed species ($^-CO_3$, adsorbed H_2O, and O_2).[61] The medium binding energy component centered at around 531.28 eV (O_b) is associated with O^{2-} ions in the oxygen deficient regions within the ZnO matrix and/or Zn−OH groups.[34] The peak located on the low binding energy side (O_a peak) on the spectrum around 530.03 eV is attributed to O^{2-} ions on the wurtzite structure of a hexagonal Zn^{2+} ion array, which is surrounded by zinc atoms with the full supplement of nearest-neighbor O^{2-} ions.[34] Hence, the O_a peak of the O 1s spectrum

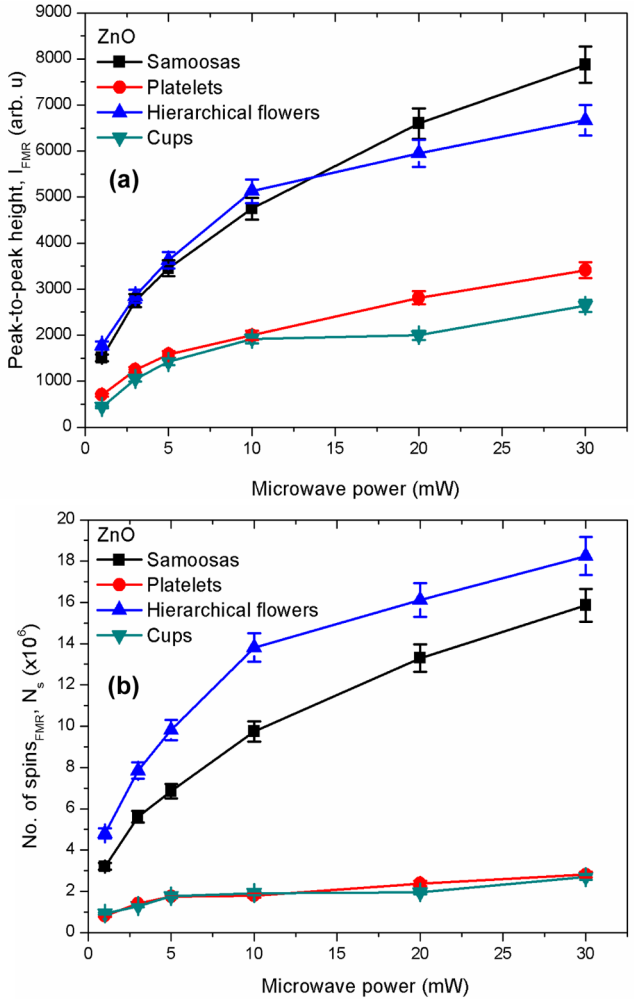

Figure 10. Evolution of (a) peak-to-peak height (I) and (b) number of spins (N_s) as a function of microwave power for as-grown ZnO nanostructures.

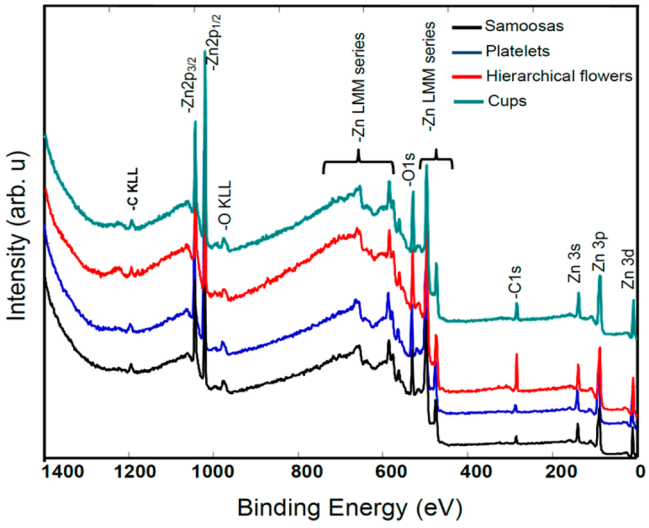

Figure 11. XPS survey scan of various ZnO nanostructures.

is associated with Zn−O bonds and the intensity of this component is a measure of the amount of oxygen atoms in fully oxidized stoichiometric surrounding. Thus, the change in the intensity of the O_b relative area may be associated with the

dx.doi.org/10.1021/am501911y | ACS Appl. Mater. Interfaces 2014, 6, 8981−8995

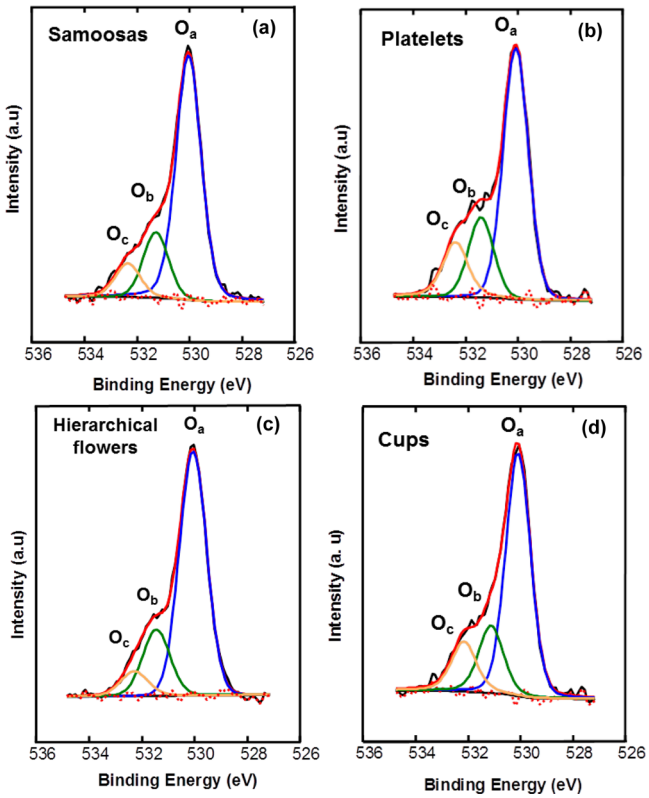

Figure 12. Experimental and fitted curves for normalized O 1s XPS spectra of various ZnO nanostructures (a) samoosas, (b) platelets, (c) hierarchical flowers and (d) cups.

concentration of oxygen vacancies (V_O).[62] From Figure 12, it can be seen that the O_b peak is present in all the samples and this indicates that there are some oxygen vacancies in all the samples. This is consistent with the observation of the Raman (Figure 5) and PL analyses (Figure 6). Remarkably, the variation of the O_b relative area is consistent with that of the FMR in all the samples. To clearly elucidate the effect of RTFM existing in ZnO in detail, we integrated the intensity ratio of O_a/O_b and the relative atom concentration ratios of O_a/Zn, (O_a+O_b)/Zn, and the relative intensity of O_a and O_b for various ZnO nanostructures and this is shown in Table 3.

It is observed from Table 3a that the relative atom concentration ratios of $(O_a + O_b)$/Zn are greater than 1.0 denoting excess oxygen in the bulk of ZnO nanostructures. This excess oxygen is also evident in Table 3b, after sputtering with Ar ions for cleaning surface contaminants. Therefore, the XPS analysis confirmed that the ZnO structures also contain V_{Zn}, which were deduced to play a role inducing the green emission together with V_O^+ as observed from the PL analysis. These results are in agreement with the observation of amorphous structure of intergranular layers and deficit of zinc or oxygen atoms observed by Straumal et al.[63,64] and Guglieri et al.[65]

To further verify this proposal and complement the EPR analyses, the field dependence of magnetization at room-temperature for various ZnO nanostructures was studied in the external applied magnetic field range of ±14 kOe using a vibrating sample magnetometer (VSM). For magnetization versus magnetic field (*M-H*) measurements (Figure 13), the samples were taken in a powder form and the diamagnetic contribution from the sample holder was subtracted.[51] It can be seen in Figure 13 that all samples exhibit clear hysteresis loops (see insets), suggesting explicitly a room temperature ferromagnetic-like (RTFM) component. These clear hysteresis loops show the typical features of ferromagnetism (or magnetic parameters) such as remanence (M_R), coercivity (H_C), saturation magnetization (M_S), squareness of the hysteresis loops (M_R/M_S) and experimental magnetic moments (μ) calculated from *M-H* data (Table 4). These values, especially the coecivity are agreement with the previous results.[13,25,65] The experimental magnetic moments per molecule in Bohr magneton (μ_B) were estimated using the formula $\mu = M_w M_S / 5585$ where M_w is the molecular weight of the compound.[66] M_R/M_S indicates the ease with which the direction of M is reoriented toward the nearest easy axis magnetization direction after the applied field is removed. The magnetic properties of materials depend on several factors which may include synthesis method, size and shape of the particles. Therefore, our results show that the magnetic properties of the samples are dependent on the shape of the studied samples. It is interesting to point out that these features are much more significant for the hierarchical flowers and samoosas as compared to their counterparts, platelet- and "cup-like" structures (Table 4). This is consistent with the EPR and PL analyses which revealed that both hierarchical flowers and samoosas contain more V_{Zn} and V_O^+. This type of magnetic response in other undoped oxides have also been reported previously.[16,18,67] Several studies have proposed the F^+ center exchange mechanism due to extended bound magnetic polarons (BMP) which overlap to create a spin-split impurity band. This mechanism could elucidate the related RTFM induced by point defects such as oxygen vacancies in some undoped oxides. Uncontrolled formation of lattice defects can generate carriers that mediate ferromagnetism. The F^+ centers are mainly the electrons in the singly occupied oxygen vacancies lying deep in the gap which can favor ferromagnetic ordering. Thus, it interesting to indicate that there appears to be a flawless-link between the ferromagnetism, V_{Zn}, and V_O^+ which indicates that V_{Zn} and V_O^+ play a vital role in triggering the RTFM in ZnO nanostructures. However, the role of point defects such as V_O^+ or V_{Zn} in mediating the FM interactions in undoped ZnO still requires further theoretical and experimental investigations.

To study the thermal stability of different ZnO nanostructures, thermogravimetric analysis (TGA) was carried out in air.

Table 3a. Chemical state of oxygen and zinc in different ZnO nanostructures before surface sputtering with Ar^+ ions

Structures	O_a position (eV)	O_b position (eV)	O_c position (eV)	O_a/O_b	O_a/Zn	(O_a+O_b)/Zn	Relative intensity of O_a (%)	Relative intensity of O_b (%)
Samoosas	530.03 ± 0.05	531.28 ± 0.69	532.35 ± 0.78	3.89 ± 0.38	1.07 ± 0.07	1.35 ± 0.13	71.70 ± 4.45	18.43 ± 0.67
Platelets	530.08 ± 0.04	531.41 ± 0.39	532.39 ± 0.44	3.11 ± 0.59	0.95 ± 0.05	1.26 ± 0.24	63.65 ± 3.31	20.46 ± 2.91
Hierarchical flowers	530.06 ± 0.07	531.45 ± 0.08	532.28 ± 0.20	3.55 ± 1.32	1.08 ± 0.06	1.38 ± 0.65	71.83 ± 4.38	20.25 ± 6.21
Cups	530.09 ± 0.46	531.12 ± 0.15	532.16 ± 0.11	3.36 ± 0.21	0.98 ± 0.04	1.25 ± 0.23	65.44 ± 2.78	19.48 ± 2.74

Table 3b. Chemical state of oxygen and zinc in different ZnO nanostructures after surface sputtering with Ar^+ ions

Samoosas	529.96 ± 0.02	531.15 ± 0.09	532.09 ± 0.22	4.75 ± 1.58	1.10 ± 0.06	1.33 ± 0.44	73.32 ± 3.95	15.43 ± 4.28
Platelets	530.33 ± 0.07	531.65 ± 0.19	532.60 ± 0.16	3.61 ± 0.36	1.03 ± 0.03	1.32 ± 0.13	69.00 ± 2.24	19.12 ± 1.30
Hierarchical flowers	530.03 ± 0.09	531.16 ± 0.05	532.32 ± 0.08	4.34 ± 1.49	1.10 ± 0.13	1.35 ± 0.47	71.85 ± 8.28	16.53 ± 3.77
Cups	530.12 ± 0.06	531.34 ± 0.02	532.25 ± 0.05	4.17 ± 0.20	1.03 ± 0.02	1.28 ± 0.26	68.59 ± 1.53	16.44 ± 2.97

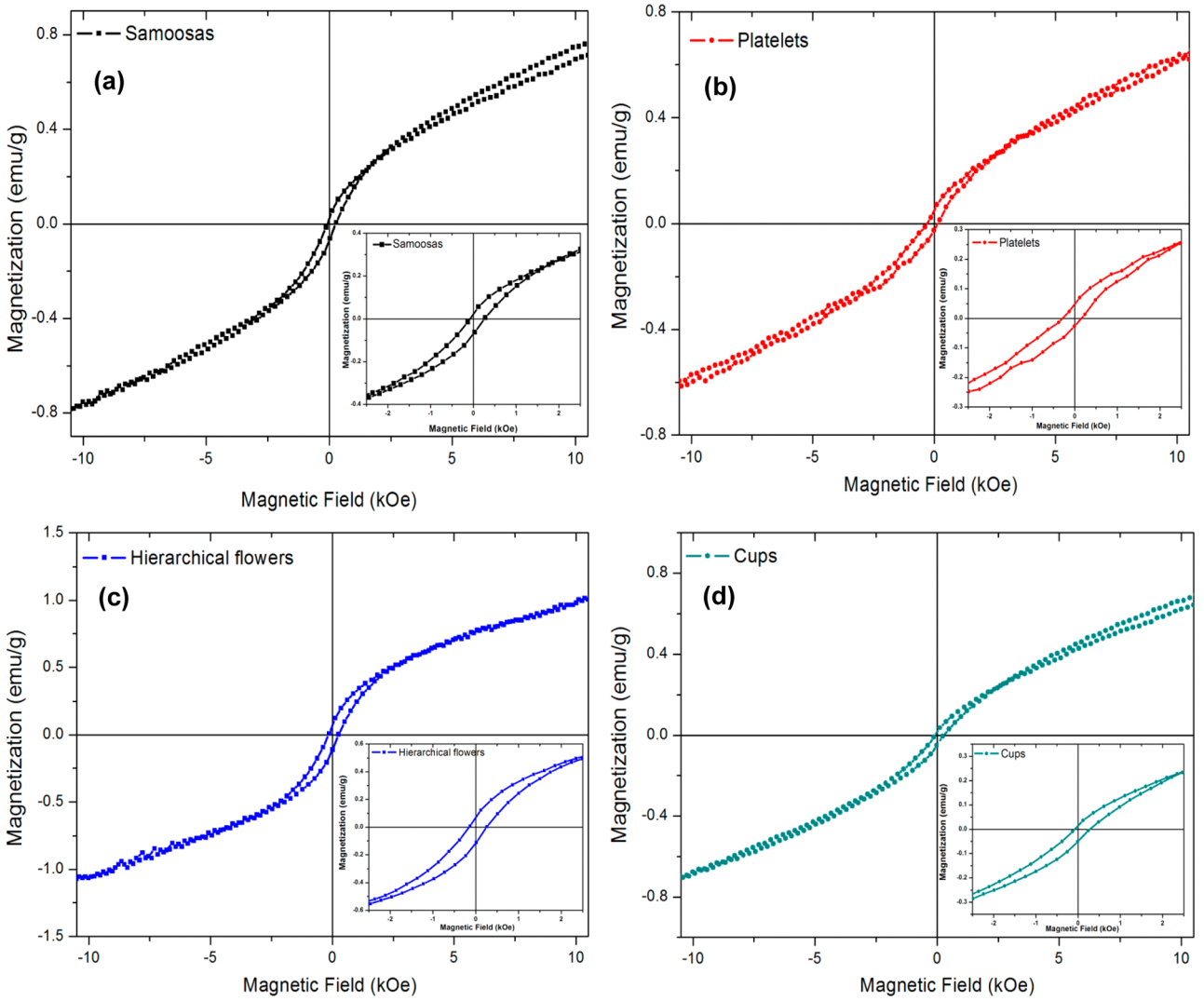

Figure 13. Hysteresis loops of various ZnO structures measured at room temperature (a) samoosas, (b) platelets, (c) hierarchical flowers, and (d) cups. Note: insets show zoomed-in hysteresis loops at low fields.

Table 4. Coercive Fields (H_C), Remanent Magnetizations (M_R), and Saturation Magnetizations (M_S) of Various ZnO Nanostructures

materials	H_C (Oe) ± 5.00	M_R ($\times 10^{-4}$) (emu/g) ± 0.01	M_S (emu/g) ± 0.06	$\mu(\mu_B)$ ± 0.0005
samoosas	197.42	2.17	0.87	0.0127
platelets	115.06	1.55	0.81	0.0118
hierarchical flower	213.62	7.77	1.15	0.0168
cups	189.58	1.46	0.82	0.0120

As shown in Figure 14, the samoosas and cups show a weight loss of approximately 1.5% when heated from 50 to 150 °C, whereas the platelets and hierarchical structures display negligible weight loss (<1%). The initial weight loss for all the structures between 50 and 150 °C is ascribed to the removal of physically and chemically adsorbed water molecules. In the temperature range between 150 and 450 °C, an increase in weight loss is registered, an effect that is likely due to the decomposition of hydroxide groups.[68] Above 500 °C, there is no significant weight loss, indicating no further decomposition above this temperature.[69] A slight weight increase observed above 500 °C might be due to the change of the crystal structure, i.e., the crystallization of ZnO. This denotes that the crystallization of ZnO nanostructures occurred at temperatures over 500 °C. Chen et al.[70] also observed a large exothermic peak exhibited at 490 °C, due to the crystallization of ZnO.

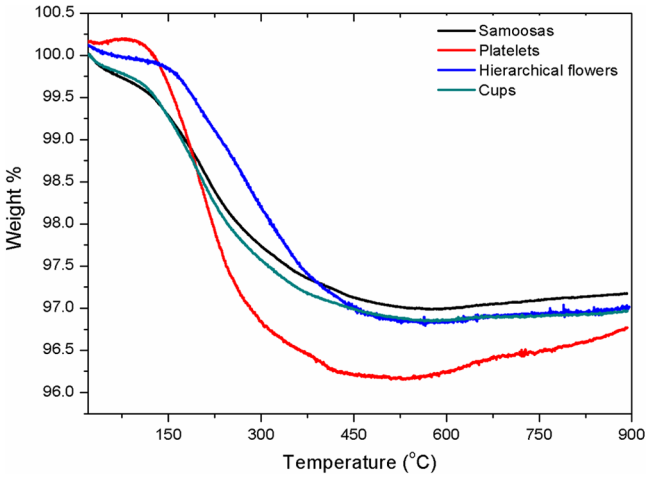

Figure 14. Thermogravimetric analysis of ZnO nanostructures.

4. CONCLUSIONS

In summary, various types of ZnO nanostructures with controllable morphologies, which are composed of "rod-like" structure, samoosas, platelets, cups, and hierarchical "flower-like" structures were successfully synthesized using a microwave assisted hydrothermal method. Thermal analysis revealed that the ZnO nanostructures are highly pure and stable. XRD and HR-TEM analyses showed that ZnO nanostructures are polycrystalline with the wurtzite structure and no other secondary phases. PL, EPR, VSM, and XPS results showed that both V_O^+ and V_{Zn}, which are located mainly near the surface of ZnO, play a significant role in modulating ferromagnetism in undoped ZnO nanostructures. Intense ferromagnetic signals, with effective g-values at $g > 2.0$ and exhibiting a shape/morphology-dependent sextet hyperfine structure, were observed. These hyperfine structures were shown to be microwave power-dependent. A novel LFMA signal was observed, and its strength was found to increase with increasing microwave power. Our findings also showed that the FMR signal and N_s improves with microwave absorption. The RTFM observed at high temperatures suggested that these structures are stable even at elevated temperatures. The observed intrinsic RTFM makes these ZnO nanostructures possible candidates for future spintronic devices.

■ ASSOCIATED CONTENT

Supporting Information

Additional experimental details related to magnetization. The elemental analyses of the ZnO nanostructures obtained by energy dispersive X-ray spectroscopy (EDS) and magnetic properties measured by EPR at various temperatures (300−450 K). HR-SEM images of the re-produced ZnO nanostructures. This material is available free of charge via the Internet at http://pubs.acs.org.

■ AUTHOR INFORMATION

Corresponding Authors

*Dr. David Motaung. Tel: (+27) 12 841 4775. Fax: (+27) 12 841 2229. E-mail: dmotaung@csir.co.za.
*Dr. Gugu Mhlongo. Tel: (+27) 12 841 3935. Fax: (+27) 12 841 2229. E-mail: gmhlongo@csir.co.za.
*Dr. Steven Nkosi. Tel: (+27) 12 841 3876. Fax: (+27) 12 841 2229. E-mail: snkosi@csir.co.za.

Notes

The authors declare no competing financial interest.

■ ACKNOWLEDGMENTS

This work was supported by the Department of Science and Technology and Council for Scientific and Industrial Research (Project Nos: HGER28P and HGER27S). The authors are thankful to Dr. J. Wesley-Smith and Mrs. T. Xuma for HR-TEM analysis.

■ REFERENCES

(1) Alammar, T.; Mudring, A. V. Facile Ultrasound-Assisted Synthesis of ZnO Nanorods in an Ionic Liquid. *Mater. Lett.* **2009**, *63*, 732−735.
(2) Rai, P.; Kwak, W. K.; Yu, Y. T. Solvothermal Synthesis of ZnO Nanostructures and Their Morphology-Dependent Gas-Sensing Properties. *ACS Appl. Mater. Interfaces* **2013**, *5*, 3026−3032.
(3) Hu, T.; Li, F.; Yuan, K.; Chen, Y. Efficiency and Air-Stability Improvement of Flexible Inverted. *ACS Appl. Mater. Interfaces* **2013**, *5*, 5763−5770.
(4) Nkosi, S. S.; Kortidis, I.; Motaung, D. E.; Malgas, G. F.; Keartland, J.; Sideras-Haddad, E.; Forbes, A.; Mwakikunga, B. W.; Kiriakidis, G.; Sinha-Ray, S. Orientation-Dependent Low Field Magnetic Anomalies and Room-Temperature Spintronic Material—Mn Doped ZnO Films by Aerosol Spray Pyrolysis. *J. Alloys Compd.* **2013**, *579*, 485−494.
(5) Lawes, G.; Risbud, A. S.; Ramirez, A. P.; Seshadri, R. Absence of Ferromagnetism in Co and Mn Substituted Polycrystalline ZnO. *Phys. Rev. B* **2005**, *71*, 045201−045205.
(6) Knut, R.; Wikberg, J. M.; Lashgari, K.; Coleman, V. A.; Westin, G.; Svedlindh, P.; Karis, O. Magnetic and Electronic Characterization of Highly Co-doped ZnO: An Annealing Study at the Solubility Limit. *Phys. Rev. B* **2010**, *82*, 094438−094444.
(7) Ghosh, S.; Khan, G. G.; Varma, S.; Mandal, K. Influence of Film Thickness and Oxygen Partial Pressure on Cation-Defect-Induced Intrinsic Ferromagnetic Behavior in Luminescent p-Type Na-Doped ZnO Thin Films. *ACS Appl. Mater. Interfaces* **2013**, *5*, 2455−2461.
(8) Dietl, T.; Ohno, H.; Matsukura, F. Hole-Mediated Ferromagnetism in Tetrahedrally Coordinated Semiconductors. *Phys. Rev. B* **2001**, *63*, 195205−195225.
(9) Coey, J. M. D.; Venkatesan, M.; Fitzgerald, C. B. Donor Impurity Band Exchange in Dilute Ferromagnetic Oxides. *Nat. Mater.* **2005**, *4*, 173−179.
(10) Tietze, T.; Gacic, M.; Schütz, G.; Jakob, G.; Brück, S.; Goering, E. XMCD Studies on Co and Li Doped ZnO Magnetic Semiconductors. *New J. Phys.* **2008**, *10*, 055009−0550026.
(11) Gacic, M.; Jakob, G.; Herbort, C.; Adrian, H.; Tietze, T.; Brück, S.; Goering, E. Magnetism of Co-Doped ZnO Thin Films. *Phys. Rev. B* **2007**, *75*, 205206−205213.
(12) Xu, Q.; Schmidt, H.; Hartmann, L.; Hochmuth, H.; Lorenz, M.; Setzer, A.; Esquinazi, P.; Meinecke, C.; Grundmann, M. Room Temperature Ferromagnetism in Mn-doped ZnO Films Mediated by Acceptor Defects. *Appl. Phys. Lett.* **2007**, *91*, 092503−092505.
(13) García, M. A.; Merino, J. M.; Pinel, E. F.; Quesada, A.; de la Venta, J.; González, M. L. R.; Castro, G. R.; Crespo, P.; Llopis, J.; González-Calbet, J. M.; Hernando, A. Magnetic Properties of ZnO Nanoparticles. *Nano Lett.* **2007**, *7*, 1489−1494.
(14) Sundaresan, A.; Bhargavi, R.; Rangarajan, N.; Siddesh, U.; Rao, C. N. R. Ferromagnetism as a Universal Feature of Nanoparticles of the Otherwise Nonmagnetic Oxides. *Phys. Rev. B* **2006**, *74*, 161306−161309.
(15) Liu, W.; Li, W.; Hu, Z.; Tang, Z.; Tang, X. Effect of Oxygen Defects on Ferromagnetic of Undoped ZnO. *J. Appl. Phys.* **2011**, *110*, 013901−013905.
(16) Venkatesan, M.; Fitzgerald, C. B.; Coey, J. M. D. Unexpected Magnetism in a Dielectric Oxide. *Nature* **2004**, *430*, 630−630.
(17) Ghosh, S.; Khan, G. G.; Mandal, K. Defect-Driven Magnetism in Luminescent n/p-Type Pristine and Gd-Substituted SnO_2 Nano-

crystalline Thin Films. *ACS Appl. Mater. Interfaces* **2012**, *4*, 2048−2056.
(18) Panigrahy, B.; Aslam, M.; Misra, D. S.; Ghosh, M.; Bahadur, D. Defect-Related Emissions and Magnetization Properties of ZnO Nanorods. *Adv. Funct. Mater.* **2010**, *20*, 1161−1165.
(19) Khalid, M.; Ziese, M.; Setzer, A.; Esquinazi, P.; Lorenz, M.; Hochmuth, H.; Grundmann, M.; Spemann, D.; Butz, T.; Brauer, G.; Anwand, W.; Fischer, G.; Adeagbo, W. A.; Hergert, W.; Ernst, A. Defect-induced Magnetic Order in Pure ZnO Films. *Phys. Rev. B* **2009**, *80*, 035331−035335.
(20) Dev, P.; Zeng, H.; Zhang, P. Defect-Induced Magnetism in Nitride and Oxide Nanowires: Surface Effects and Quantum Confinement. *Phys. Rev. B* **2010**, *82*, 165319−165324.
(21) Chakrabarty, A.; Patterson, C. H. Defect Trapped Electrons and Ferromagnetic Exchange in ZnO. *Phys. Rev. B* **2011**, *84*, 054441−054455.
(22) Céspedes, E.; Laguna-Marco, M. A.; Jiménez-Villacorta, F.; Chaboy, J.; Boada, R.; Guglieri, C.; de Andrés, A.; Prieto, C. On the Origin of the Magnetism of Mn-Zn-O Systems: Structural, Electronic, and Magnetic Study of Exotic $MnO_{2-\delta}$/ZnO Thin Films. *J. Phys. Chem. C* **2011**, *115*, 24092−24101.
(23) Barla, A.; Schmerber, G.; Beaurepaire, E.; Dinia, A.; Bieber, H.; Colis, S.; Scheurer, F.; Kappler, J. P.; Imperia, P.; Nolting, F.; Wilhelm, F.; Rogalev, A.; Müller, D.; Grob, J. J. Paramagnetism of the Co Sublattice in Ferromagnetic $Zn_{1-x}Co_xO$ Films. *Phys. Rev. B* **2007**, *76*, 125201−125205.
(24) Keavney, D. J.; Buchholz, D. B.; Ma, Q.; Chang, R. P. H. Where Does the Spin Reside in Ferromagnetic Cu-doped ZnO? *Appl. Phys. Lett.* **2007**, *91*, 012501−012503.
(25) Chaboy, J.; Boada, R.; Piquer, C.; Laguna-Marco, M. A.; García-Hernández, M.; Carmona, N.; Llopis, J.; Ruìz-González, M. L.; González-Calbet, J.; Fernández, J. F.; García, M. A. Evidence of Intrinsic Magnetism in Capped ZnO Nanoparticles. *Phys. Rev. B* **2010**, *82*, 064411−064419.
(26) Guglieri, C.; Laguna-Marco, M. A.; Garcìa, M. A.; Carmona, N.; Ceś pedes, E.; Garcìa-Hernández, M.; Espinosa, A.; Chaboy, J. XMCD Proof of Ferromagnetic Behaviour in ZnO Nanoparticles. *J. Phys. Chem. C* **2012**, *116*, 6608−6614.
(27) Guglieri, C.; Céspedes, E.; Espinosa, A.; Laguna-Marco, M. Á.; Carmona, N.; Takeda, Y.; Okane, T.; Nakamura, T.; García-Hernández, M.; García, M. Á.; Chaboy, J. Evidence of Oxygen Ferromagnetism in ZnO Based Materials. *Adv. Funct. Mater.* **2014**, *24*, 2094−2100.
(28) García, M. A.; Pinel, E. F.; de la Venta, J.; Quesada, A.; Bouzas, V.; Fernández, J. L.; Romero, J. L.; Martn-González, M. S.; Costa-Krämer, J. L. Sources of Experimental Errors in the Observation of Nanoscale Magnetism. *J. Appl. Phys.* **2009**, *105*, 013925−013931.
(29) Rai, P.; Jo, J.-N.; Lee, I.-H.; Yu, Y.-T. Fabrication of Flower-Like ZnO Microstructures From ZnO Nanorods and Their Photoluminescence Properties. *Mater. Chem. Phys.* **2010**, *124*, 406−412.
(30) Zhang, J. L.; Sun, J.; Yin, H.; Su, C.; Liao, C. S.; Yan, C. H. Control of ZnO Morphology via a Simple Solution Route. *Chem. Mater.* **2002**, *14*, 4172−4177.
(31) Lupan, O.; Chow, L.; Chai, G. Y.; Roldan, B.; Naitabdi, A.; Schulte, A.; Heinrich, H. Nanofabrication and Characterization of ZnO Nanorod Arrays and Branched Microrods by Aqueous Solution Route and Rapid Thermal Processing. *Mater. Sci. Eng., B* **2007**, *145*, 57−66.
(32) Wu, J. J.; Liu, S. C. Catalyst-Free Growth and Characterization of ZnO Nanorods. *J. Phys. Chem. B* **2002**, *106*, 9546−9551.
(33) Exarhos, G. J.; Sharma, S. K. Influence of Processing Variables on the Structure and Properties of ZnO Films. *Thin Solid Films* **1995**, *270*, 27−32.
(34) Mhlongo, G. H.; Motaung, D. E.; Nkosi, S. S.; Swart, H. C.; Malgas, G. F.; Hillie, K. T.; Mwakikunga, B. W. Temperature-Dependence on the Structural, Optical, and Paramagnetic Properties of ZnO Nanostructures. *Appl. Surf. Sci.* **2014**, *293*, 62−70.
(35) Zhang, X.; Xia, Y.; He, T. Tuning Photoluminescence Properties of ZnO Nanorods via Surface Modification. *Mater. Chem. Phys.* **2012**, *137*, 622−627.
(36) Mahamuni, S.; Borgohain, K.; Bendre, B. S.; Leppert, V. J.; Risbud, S. H. Spectroscopic and Structural Characterization of Electrochemically Grown ZnO Quantum Dots. *J. Appl. Phys.* **1999**, *85*, 2861−2865.
(37) Zeng, H. B.; Cai, W. P.; Hu, J. L.; Duan, G. T.; Liu, P. S. Violet Photoluminescence from Shell Layer of Zn/ZnO Core-Shell Nanoparticles Induced By Laser Ablation. *Appl. Phys. Lett.* **2006**, *88*, 171910−171912.
(38) Vanheusden, K.; Warren, W. L.; Seager, C. H.; Tallant, D. R.; Voigt, J. A.; Gnade, B. E. Mechanisms Behind Green Photoluminescence in ZnO Phosphor Powders. *J. Appl. Phys.* **1996**, *79*, 7983−7990.
(39) Sun, Y. G.; Fuge, M.; Fox, N. A.; Riley, D. J.; Ashfold, M. N. R. Synthesis of Aligned Arrays of Ultrathin ZnO Nanotubes on a Si Wafer Coated with a Thin ZnO Film. *Adv. Mater.* **2005**, *17*, 2477−2481.
(40) Djurišić, A. B.; Leung, Y. H.; Tam, K. H.; Hsu, Y. F.; Ding, L.; Ge, W. K.; Zhong, Y. C.; Wong, K. S.; Chan, W. K.; Tam, H. L.; Cheah, K. W.; Kwok, W. M.; Phillips, D. L. Defect Emissions in ZnO Nanostructures. *Nanotechnology* **2007**, *18*, 095702−095711.
(41) Lin, C. Y.; Wang, W. H.; Lee, C.-S.; Sun, K. W.; Suen, Y. W. Magnetophotoluminescence Properties of Co-doped ZnO Nanorods. *Appl. Phys. Lett.* **2009**, *94*, 151909−1519011.
(42) Wang, Y. G.; Lau, S. P.; Zhang, X. H.; Hng, H. H.; Lee, H. W.; Yu, S. F.; Tay, B. K. Enhancement of Near-Band-Edge Photoluminescence from ZnO Films by Face-to-Face Annealing. *J. Cryst. Growth* **2003**, *259*, 335−342.
(43) Janotti, A.; Van de Walle, C. G. Native Point Defects in ZnO. *Phys. Rev. B* **2007**, *76*, 165202−165223.
(44) Reynolds, D. C.; Look, D. C.; Jogai, B.; Van Nostrand, J. E.; Jones, R.; Jenny, J. Source of the Yellow Luminescence Band in GaN Grown by Gas-Source Molecular Beam Epitaxy and the Green Luminescence Band in Single Crystal ZnO. *Solid State Commun.* **1998**, *106*, 701−704.
(45) Dijken, A. V.; Meulenkamp, E. A.; Vanmaekelbergh, D.; Meijerink, A. The Luminescence of Nanocrystalline ZnO Particles: The Mechanism of the Ultraviolet and Visible Emission. *J. Lumin.* **2000**, *87*, 454−456.
(46) Cross, R. B. M.; De Souza, M. M.; Sankara Narayanan, E. M. A Low Temperature Combination Method for the Production of ZnO Nanowires. *Nanotechnology* **2005**, *16*, 2188−2192.
(47) Chen, C.-W.; Chen, K.-H.; Shen, C.-H.; Ganguly, A.; Chen, L.-C.; Wu, J.-J.; Wen, H.-I.; Pong, W.-F. Anomalous Blue-Shift in Emission Spectra of ZnO Sanorods with Sizes Beyond Quantum Confinement Regime. *Appl. Phys. Lett.* **2006**, *88*, 241905−241907.
(48) Zhang, X.; Li, X. M.; Chen, T. L.; Bian, J. M.; Zhang, C. Y. Structural and Optical Properties of $Zn_{1-x}Mg_xO$ Thin Films Deposited by Ultrasonic Spray Pyrolysis. *Thin Solid Films* **2005**, *492*, 248−252.
(49) Reddy, A. J.; Kokila, M. K.; Nagabhushana, H.; Sharma, S. C.; Raod, J. L.; Shivakumara, C.; Nagabhushana, B. M.; Chakradhar, R. P. S. Structural, EPR, Photo and Thermoluminescence Properties of ZnO:Fe Nanoparticles. *Mater. Chem. Phys.* **2012**, *133*, 876−883.
(50) Banerjee, S.; Mandal, M.; Gayathri, N.; Sardar, M. Enhancement of Ferromagnetism Upon Thermal Annealing in Pure ZnO. *Appl. Phys. Lett.* **2007**, *91*, 182501−182504.
(51) Xu, X.; Xu, C.; Dai, J.; Hu, J.; Li, F.; Zhang, S. Size Dependence of Defect-Induced Room Temperature Ferromagnetism in Undoped ZnO Nanoparticles. *J. Phys. Chem. C* **2012**, *116*, 8813−8818.
(52) Sagar, R. V.; Buddhudu, S. Synthesis and Magnetic Behaviour of Mn:ZnO Nanocrystalline Powders. *Spectrochim. Acta, Part A* **2010**, *75*, 1218−1222.
(53) Djurišić, A. B.; Choy, W. C. H.; Roy, V. A. L.; Leung, Y. H.; Kwong, C. Y.; Cheah, K. W.; Gundu Rao, T. K.; Chan, W. K.; Fei Lui, H.; Surya, C. Photoluminescence and Electron Paramagnetic Resonance of ZnO Tetrapod Structures. *Adv. Funct. Mater.* **2004**, *14*, 856−864.
(54) Morazonni, F.; Scotti, R.; Di Nola, P.; Milani, C.; Narducci, D. Electron Paramagnetic Resonance Study of the Interaction of the ZnO

Surface with Air and Air-Reducing Gas Mixtures. *J. Chem. Soc., Faraday Trans.* **1992**, *88*, 1691−1694.
(55) Garces, N. Y.; Wang, L.; Bai, L.; Gijes, N. C.; Halliburton, L. E.; Cantwell, G. Role of Copper in the Green Luminescence from ZnO Crystals. *Appl. Phys. Lett.* **2002**, *81*, 622−624.
(56) Smith, J. M.; Vehse, W. E. ESR of Electron Irradiated ZnO Confirmation of the F^+ Center. *Phys. Lett. A* **1970**, *31*, 147−148.
(57) Taylor, A. L.; Filipovich, G.; Lindeberg, G. K. Electron Paramagnetic Resonance Associated with Zn Vacancies in Neutron-Irradiated ZnO. *Solid State Commun.* **1970**, *8*, 1359−1361.
(58) Galland, D.; Herve, A. ESR Spectra of the Zinc Vacancy in ZnO. *Phys. Lett.* **1970**, *33A*, 1−2.
(59) Gavi, H.; Ngom, B. D.; Beye, A. C.; Strydom, A. M.; Srinivasu, V. V.; Chaker, M.; Manyala, N. Low-field Microwave Absorption in Pulse Laser Deposited FeSi Thin Film. *J. Magn. Magn. Mater.* **2012**, *324*, 1172−1176.
(60) Pan, F.; Song, C.; Liu, X. J.; Yang, Y. C.; Zeng, F. Ferromagnetism and Possible Application in Spintronics of Transition-Metal-Doped ZnO Films. *Mater. Sci. Eng., R* **2008**, *62*, 1−35.
(61) Major, S.; Kumar, S.; Bhatnagar, M.; Chopra, K. L. Effect of Hydrogen Plasma Treatment on Transparent Conducting Oxides. *Appl. Phys. Lett.* **1986**, *49*, 394−399.
(62) Szorenyi, T.; Laude, L. D.; Bertoti, I.; Kantor, Z.; Geretovszky, Z. Excimer Laser Processing of Indium-Tin-Oxide Films: An Optical Investigation. *J. Appl. Phys.* **1995**, *78*, 6211−6219.
(63) Straumal, B. B.; Mazilkin, A. A.; Protasova, S. G.; Myatiev, A. A.; Straumal, P. B.; Goering, E.; Baretzky, B. Amorphous Grain Boundary Layers in the Ferromagnetic Nanograined ZnO Films. *Thin Solid Films* **2011**, *520*, 1192−1194.
(64) Straumal, B. B.; G, P. S.; Mazilkin, A. A.; Baretzky, B.; Myatiev, A. A.; Straumal, P. B.; Tiezte, T.; Schütz, G.; Goering, E. Amorphous Interlayers Between Crystalline Grains in Ferromagnetic ZnO Films. *Mater. Lett.* **2012**, *71*, 21−24.
(65) Guglieri, C.; Espinosa, A.; Carmona, N.; Laguna-Marco, M. Á.; Céspedes, E.; Ruíz-González, M. L.; González-Calbet, J.; García-Hernández, M.; García, M. Á.; Chaboy, J. Relationship between the Magnetic Properties and the Formation of a ZnS/ZnO Interface in *S*—Capped ZnO Nanoparticles and ZnS−ZnO Thin Films. *J. Phys. Chem. C* **2013**, *117*, 12199−12209.
(66) Abdallah, H. M. I.; Moyo, T. Structural and Magnetic Studies of $(Mg, Sr)_{0.2}Mn_{0.1}Co_{0.7}Fe_2O_4$ Nanoferrites. *J. Alloys Compd.* **2013**, *562*, 156−163.
(67) Ghosh, S.; Khan, G. G.; Das, B.; Mandal, K. Vacancy-Induced Intrinsic d^0 Ferromagnetism and Photoluminescence in Potassium Doped ZnO Nanowires. *J. Appl. Phys.* **2011**, *109*, 123927−123932.
(68) Motaung, D. E.; Malgas, G. F.; Arendse, C. J.; Mavundla, S. E. Determination of the Structure, Morphology and Complex Refractive Index in ZnO-Nanopencils/P3HT Hybrid Structures. *Mater. Chem. Phys.* **2012**, *135*, 401−410.
(69) Patil, R. P.; Joshi, S. S. Polymerized Organic−Inorganic Synthesis of Nanocrystalline Zinc Oxide. *Mater. Chem. Phys.* **2007**, *105*, 354−361.
(70) Chen, K. J.; Fang, T. H.; Hung, F. Y.; Ji, L. W.; Chang, S. J.; Young, S. J.; Hsiao, Y. J. The Crystallization and Physical Properties of Al-Doped ZnO Nanoparticles. *Appl. Surf. Sci.* **2008**, *254*, 5791−5795.